Mechanistic and Thermodynamic Insights into Anion Exchange by Green Rust

Myriam I Agnel, Sylvain Grangeon, François Fauth, Erik Elkaim, Francis Claret, Marjorie Roulet, Fabienne Warmont, Christophe Tournassat

Mechanistic and thermodynamic insights into anion exchange by green rust

Myriam I. Agnel[*,1], *Sylvain Grangeon*[1,2], *François Fauth*[3], *Erik Elkaïm*[4], *Francis Claret*[2], *Marjorie Roulet*[5], *Fabienne Warmont*[5], *Christophe Tournassat*[1,2,6]

[1] Univ. Orléans, CNRS, BRGM, ISTO, UMR 7327, F-45071, Orléans, France

[2]BRGM, 3 Avenue Claude Guillemin, 45060 Orléans, France

[3]CELLS – ALBA Synchrotron, Carrer de la Llum, 2-26, 08290 Cerdanyola del Vallès, Barcelona, Spain

[4]Synchrotron SOLEIL, L'Orme des Merisiers, 91190 Saint Aubin, France

[5]ICMN, UMR 7374, CNRS/Université d'Orléans, 1 Rue de la Ferollerie, 45071 Orléans, France

[6]Energy Geoscience Division, Lawrence Berkeley National Laboratory, 1 Cyclotron Rd, Berkeley, CA 94720, USA

KEYWORDS: Green rust, Anion exchange, Fougerite, Layered Double Hydroxide.

ABSTRACT

Fougerite is a naturally-occurring green rust, i.e. a layered double hydroxide (LDH) containing iron (Fe). Fougerite was identified in natural settings such as hydromorphic soils. It is one of the few inorganic materials with large anion adsorption capacity that stems from the presence of isomorphic substitutions of Fe^{2+} by Fe^{3+} in its layers. The importance of anion adsorption in the interlayer of LDH has often been highlighted, but we are still missing a mechanistic understanding and a thermodynamic framework to predict anion uptake by green rust. We combined laboratory and *in operando* synchrotron X-ray diffraction and scattering experiments with geochemical modeling to contribute to filling this gap. We showed that the overall exchange process in green rusts having nanometer and micrometer sizes can be seen as a simple anion exchange mechanism without dissolution-recrystallization or interstratification processes. A thermodynamic model of ion exchange, based on the Rothmund and Kornfeld convention, made it possible to predict the interlayer composition in a large range of conditions. This multiscale characterization can serve as a starting point for the building of robust and mechanistic geochemical models that will allow predicting the role of green rust on the geochemical cycle of ions, including nutrients, in soils.

30 ABSTRACT ART

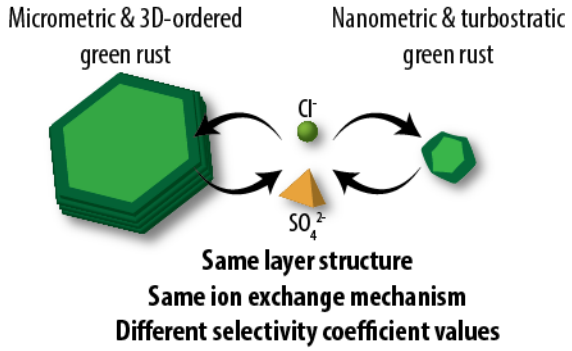

31
32

TEXT

INTRODUCTION

Green rust (GR) is a layered double hydroxide (LDH) that contains Fe^{2+} and Fe^{3+}, and which is found both in engineered and natural environments.[1–3] Fougerite, the naturally-occurring form of green rust, has been identified in several settings such as hydromorphic soils and river streams.[1,4–8] In the following "Fougerite" will be used to refer specifically to the mineral, while "green rust" will be used both to refer to synthetic samples and to discuss properties that are common to Fougerite and synthetic samples.

Where present, green rust exerts a strong influence on the mobility of nutrients, transition metals, and actinides through adsorption, incorporation, and redox reactions.[1,2,9–15] In addition, it is a precursor of magnetite, which is another reactive mineral.[1,12,16] As a consequence of its exceptional reactivity, green rust is envisioned as a potential material for water treatment, either through degradation or sorption of anionic contaminants.[14,17] The sorption and redox properties of green rust are due to its crystal structure. The ideal structural formula of green rust is $[Fe^{2+}_{(1-x)}Fe^{3+}_{x}(OH)_2]^{+x} \cdot [x/n\ A^{-n} \cdot m\ H_2O]^{-x}$, where iron and hydroxyl groups form positively charged layers, which are stacked and separated from each other by hydrated interlayer anions A^{-n}.[1,3] n is the charge of the anion, and m depends on factors such as relative humidity and nature of the anion.[15,18] Interlayer anions can undergo exchange reactions with the surrounding pore water, thus explaining the anion sorption capability of these materials.[2,14,15] Layers from natural and synthetic samples also frequently contain isomorphic substitution of Fe^{2+} and Fe^{3+} by foreign cations such as Al^{3+}, Mg^{2+}, Ni^{2+}, or Zn^{2+}.[7,19,20] The sorption properties of green rust are thus apparently analogous to the sorption properties of other layered minerals such as clay minerals (*e.g,* smectite)

55 or manganese oxides, but with an opposite permanent layer charge and sorption properties directed
56 towards anions instead of cations.[21,22]

57 Inorganic materials with permanent anion adsorption capacity are scarce in nature, especially in
58 the pH range 7 to 9 that corresponds to the stability range of Fougerite.[2,23] When present, this
59 mineral could have thus a major role in anions concentration buffering capacity in soils.[15] While
60 it has been profusely demonstrated that clay minerals play a major part in the control of cation
61 retention and migration in soils, sediments and sedimentary rocks,[21] the precise role of Fougerite
62 in the dynamics of anions in natural and engineered settings is less documented.[24] This can be
63 attributed, at least in part, to the scarcity or absence of quantitative data on anion exchange
64 reactions on green rust surfaces,[2,3,25,26] which prevents a quantitative estimation using geochemical
65 modeling approaches. This paper intends to contribute filling this gap. Exchange processes on clay
66 minerals are usually quantified in the framework of the thermodynamic theory of ion exchange, in
67 which exchange selectivity coefficients are determined from batch adsorption/desorption
68 experiments.[21] Literature studies carried out on a range of layered minerals and phases (e.g., clay
69 minerals, manganese oxides, or LDH phases present in cementitious materials) have shown
70 however that a sound understanding of the mechanisms of interactions between a layer and an
71 adsorbate of interest requires a molecular-scale description of the sorption process in order to
72 distinguish true reversible adsorption mechanisms from additional uptake mechanisms such as
73 structural incorporation or co-precipitation.[2,27,28]

74 The objective of the present study was to develop a thermodynamic model for anion uptake in
75 green rust that is firmly grounded on molecular-scale foundations. Additionally, this development
76 included the quantification of the influence of particle crystallinity and size on sorption properties,
77 since previous studies proposed that these parameters may play a role.[29–31] In this view, we

synthesized two types of samples: a micrometric and defect-free green rust (micro-GR), and a nanometric and turbostratic green rust (nano-GR), both having Cl^- as the interlayer anion. Then, we characterized and quantified their sulfate (SO_4^{2-}) sorption mechanisms by combining laboratory and synchrotron experiments. Cl^- and SO_4^{2-} were chosen because of their quantitative importance in surficial waters, and because of their simple aqueous speciation.

MATERIALS AND METHODS

Anoxic conditions. All synthesis steps and laboratory experiments were conducted in a glove box (MBraun UNIlab Pro) filled with a N_2 atmosphere in order to prevent the oxidation of green rust by atmospheric O_2. All solutions were prepared with O_2-free ultrapure water (resistivity of 18.2 MΩ·cm) and analytical grade salts. The glove box O_2 volumetric concentration was regularly monitored and did not exceed 0.1 Pa. Samples used for synchrotron experiments were sealed in airtight containers in the glove box. They were stored in another N_2 atmosphere glove boxes at the synchrotron facilities until being used for the experiments.

Green rust samples. The samples were synthesized using a previously published method.[32] Briefly, a $FeCl_2$ solution (50 $g \cdot L^{-1}$) was mixed with another one of hexamminecobalt(III) chloride (CoHex, 10 $g \cdot L^{-1}$). Two samples were synthesized by varying the ratio of $FeCl_2$ to CoHex so as to produce a turbostratic and nanometric green rust, hereafter named nano-GR(Cl), and a defect-free and micrometric green rust, hereafter named micro-GR(Cl). Turbostratism is defined by the systematic occurrence of random translations parallel to the layers and/or rotations about the normal direction to the layers between successive layers. The solid aged for three days before filtration (0.22 μm) of the dispersion. This synthesis method did not require external control on

the pH, which reached green rust equilibrium pH as soon as the solid precipitated (pH range during synthesis for nano-GR(Cl)=8.3-8.6, and micro-GR(Cl)=8-8.2).[32] No additional washing was done before the solid samples were dried for one day in order to minimize side reactions, including dissolution, that could have been induced by the sharp changes in chemical conditions, which always occur during washing procedures.

The present synthesis method was chosen because it allowed for a fine-tuning of the size and amount of stacking defects. The drawback of the method was the partial substitution of Fe^{2+} by Co^{2+} in the layer.[32] However, this was not considered to be a problem because (i) the crystallographic structure of the synthesized solids was almost identical to that of Fougerite (Fig. S5), (ii) the layer charge was not influenced by the Fe^{2+} versus Co^{2+} substitution, and (iii) Fougerite has never been observed as a pure Fe^{2+}/Fe^{3+} phase in natural environments, because of isomorphic substitutions of Fe by foreign cations such as Mg, Ni, or Zn.[7,13,33]

Determination of layer structural formula and interlayer anion content. The structural formula of the studied samples was $[Fe^{2+}_{1-x-y}Fe^{3+}_{x}Co^{2+}_{y}(OH)_2]^{+x}\cdot[x/n\ A^{-n}\cdot mH_2O]^{-x}$, where $A^{-n}=Cl^-$ or SO_4^{2-}.[32] The values of *x* and *y*, which can vary between 0 and 1, were calculated from electron probe micro-analyzes (EPMA; Cameca SX Five electron microprobe). Analyses were carried out on freeze-dried samples embedded in epoxy mounts. After polishing the epoxy mount, a 10-20 nm thick carbon layer was sputter-coated on the samples. Acceleration voltage was 15 kV, beam current was 10 nA and beam width was 1-2 µm. Fe Kα and Co Kα were analyzed using a LiF (Lithium Floride) crystal, while Cl Kα and SO_4 Kα were analyzed with a LPET (Large Pentaerythritol) and a PET (Pentaerythritol) crystal respectively. Pyrite, metallic Co, Vanadinite and Celestite were used as standards for Fe, Co, Cl and SO_4 respectively. Counting times was set

to 30 s for all elements. Depending on the sample, the number of independent measurements ranged 35-61. In order to provide additional constraints on the chemical formula, the total Fe content was also quantified with a modified 1,10-phenanthroline method.[32]

Determination of the water content. The water content (m) was determined with thermogravimetric analyses (TGA) and differential thermal analysis (DTA). Samples were dried for one day in the glove box, before measurement on a Setaram TGA 92-16.18 under an Argon flux. Approximately 50 mg of powder were heated from 20 °C to 500 °C at 1 °C min^{-1}. Then, the temperature was maintained at 500 °C for 1 h before cooling. The mass loss attributed to water vaporization during the TGA measurement (ΔTG) was linked to the value of m according to:

$$m = \frac{M_{GR}}{M_w} \times \frac{\Delta TG}{m_{GR}} \quad (1)$$

where M_{GR} is the molar mass of the anhydrous GR (*i.e.* considering m=0), m_{GR} is the mass of the anhydrous sample, and M_w is the molar mass of water. Care was taken to avoid any contact with atmospheric CO_2 during sample transportation and analysis.

Transmission Electron Microscopy (TEM). TEM samples were prepared according to two different methods. In the first method, solid powders were dispersed into ultrapure water using an ultrasonic bath, and then deposited on lacey carbon films loaded on copper grids. In order to avoid as much as possible oxidation, samples were preserved in a glovebox until a quick preparation (< 5 min) under open air. Samples were then directly inserted in the TEM. In the second method, samples were embedded in Agar 100 resin and left for polymerization for 2 days in the dark. Then, 80 nm thick slices were prepared with an ultramicrotome (Reichert-Jung Ultra-

cut E) equipped with a diamond knife. The slices were deposited on lacey carbon films loaded on copper grids. TEM data were acquired using a Philips CM20 operated at 200 kV.

Diffractometric characterization of the solid phase. Two types of synchrotron experiments were conducted. In the first type, X-ray diffraction data (XRD) were recorded during in situ and time-resolved sorption experiments conducted on beamline MSPD (ALBA Synchrotron, Barcelona, Spain).[34,35] The X-ray wavelength (λ) was 0.8258 Å (15 keV). Data were collected with a Mythen detector. Green rust was loaded in polyimide capillaries sealed on both extremities using a frit-in-a-ferrule system (Idex Health & Science).[36] At the beginning of each experiment, a capillary was connected on one-side to a peristaltic pump and to the other side to a sampling pot, using silicon tubing. The flow rate of the pump was 1-2 $mL \cdot h^{-1}$. In a first step (equilibrium step), the sample was hydrated by flowing a solution of 50 $mmol \cdot L^{-1}$ NaCl at pH 8. In a second step (exchange step), a solution of 5 $mmol \cdot L^{-1}$ Na_2SO_4 and 40 $mmol \cdot L^{-1}$ NaCl at pH 8 was flowed through the capillary. A diffraction pattern was acquired every 15 s during both steps. The crystallite size was calculated using Scherrer's law (see Supplementary Data).[37] Rietveld refinements were carried out on micro-GR(Cl) with the Fullprof software,[38] using the structure models from Fougerite and magnetite.[7,39] The quality of the data modelling was quantified using the R_{exp}, R_p, R_{wp}, and goodness-of-fit (GoF) parameters, where R_p is the unweighted residual error, R_{wp} is the weighted residual error, R_{exp} is the lowest R_{wp} that can be achieved as a result of statistical noise on the data, and GoF is the squared R_{wp} to R_{exp} ratio.[40]

The second type of synchrotron experiments involved processing the high-energy X-ray scattering data of dried samples collected, at beamline CRISTAL from the SOLEIL synchrotron (Paris, France) and using previously developed methods.[36,41] The energy was 28 keV (λ = 0.4367

168 Å). An XPad hybrid pixel detector collected data between 1.2-124.5° 2θ angular range with a total
169 collection time of 30 min. Then, data were processed with the software FUSION[42] and Fourier
170 transformed to X-ray Pair Distribution Function (PDF) data with *PDFgetX3*.[43] Systematic random
171 stacking disorder (turbostratism disorder) affects the PDF by cancelling out the contribution from
172 atomic pairs formed from atoms located on distinct layers. To assess quantitatively this effect, two
173 PDF were calculated. The first one, which served as a model PDF for an ordered and micrometric
174 green rust, was calculated using the Fougerite structure model,[7] in which the number of water
175 molecules and *a* and *b* lattice parameters were adjusted to match data acquired with independent
176 methods, and in which the occupancy of layer O was set to 1. The second calculated PDF aimed
177 at mimicking the PDF of a turbostratic and nanosized green rust. For this purpose, a structure
178 model was created, in which a single Fougerite sheet was isolated in a lattice cell with *a* and *b*
179 dimensions identical to that of the ordered Fougerite but with *c* dimension expended to 30 Å to
180 cancel any correlations related to atoms located on distinct layers in the calculated PDF (up to 30
181 Å). Note that the relative atomic coordinates of all atoms were corrected correspondingly, so that
182 the layer structure remained unaffected by this operation. The drawback of using such a
183 "supercell" approach was the significant lowering of the electronic density in the cell, ρ, compared
184 to that of an actual turbostratic sample. This effect manifested itself in the calculated PDF with an
185 underestimation of the slope at low *r* values, which is a function of ρ.[40] However, this did not affect
186 the position nor the intensity of correlations, which could be compared safely to other calculated
187 or experimental data. The size of the crystallites was set to 50 Å using the "spdiameter" from
188 PDFgui. For both structures, the u_{11}, u_{22} and u_{33} anisotropic displacement parameters of Fe were
189 0.01 Å and those of interlayer species were 0.1 Å. u_{11} and u_{22} of layer O were also 0.01, but u_{33}

was set to 0.03 Å to match experimental data. Such increase in u_{33} of layer O was also observed for several other layered phases,[28,36,41,44,45] and is possibly related to layer corrugation.

Cl^- – SO_4^{2-} exchange experiments. NaCl and $NaSO_4$ stock solutions as well as mixes of these solutions were prepared so as to reach a constant Na concentration of 50 mmol·L^{-1}, and a pH value between 7 and 8. Green rust samples were dried again for one day prior to experiments. During the pre-conditioning step, about 0.2 g of nano-GR(Cl) or 0.5 g of micro-GR(Cl) were equilibrated with 200 mL of a 50 mmol·L^{-1} NaCl solution for 30 min. Then, the solution and the solid were separated by filtration (cut-off diameter of 0.22 µm). The solid was rinsed with 30-40 mL of O_2- and CO_2-free ultrapure water, and then filtrated.

During each of following steps, except rinsing, the green rust was dispersed in the solutions during 30 min, which was sufficient to attain steady state conditions for Cl^- and SO_4^{2-} concentrations based on in-situ XRD measurements of Cl^--SO_4^{2-} exchange experiments. In a first series of experiment, the green rust samples were re-dispersed with a 25 mmol·L^{-1} Na_2SO_4 solution and then filtrated. Three dispersion-filtration steps were carried out. The objective of this series of experiments was the characterization of the Cl^-– SO_4^{2-} reaction stoichiometry, with the comparison of SO_4^{2-} uptake and Cl^- release in a single step, as well as of the anion exchange capacity (AEC), with the measurement of the total amount of Cl^- released by the sample. In a second series of experiments, the solid was re-dispersed with solutions containing Cl^- and SO_4^{2-} with a total Na^+ concentration of 50 mmol·L^{-1} and then filtrated. Again, five to six dispersion-filtration steps were carried out. After those 5 to 6 steps, the solid was rinsed with a known volume of ultrapure water, and dispersed again with a 25 mmol·L^{-1} Na_2SO_4 solution and filtrated (one to two dispersion-filtration steps). The objectives of this second set of experiments were to calculate equivalent

fractions and to determine the ion exchange thermodynamic convention and, accordingly, to calculate selectivity coefficients. All details about solution concentrations and volumes are available in the electronic annex (Table S1 to S3). The mass of the filtrated solutions and their Cl^- and SO_4^{2-} concentrations were quantified by High-Performance Liquid Chromatography (HPLC; Thermo Scientific Dionex ICS-3000) at each step in order to determine the concentration of Cl^- and SO_4^{2-} in the solution, as well as in the solid by cumulative difference with the initial solid concentration.

Geochemical modeling. Experimental results were modelled with PHREEQC[46] in order to determine the selectivity coefficient (K_{ex}) of the exchange reactions. At each step, the solution was assumed to be at equilibrium with the anion exchanger composition, according to the reaction:

$$\mathbf{2\,ACl + SO_4^{2-} = A_2SO_4 + 2\,Cl^-} \quad (2)$$

where A^+ represents the anion exchanger. The ion exchange thermodynamic convention of Rothmund and Kornfeld was used to compute the exchanger composition as a function of the solution composition:[21,47]

$$K_{ex,RK} = \frac{(\mathrm{Cl^-})^2}{(\mathrm{SO_4^{2-}})} \left(\frac{E_{\mathrm{SO4}}}{{E_{\mathrm{Cl}}}^2}\right)^{1/\beta} \quad (3)$$

where values in round brackets represent activities in solution, β is an empirical parameter, and E_i is the equivalent fraction of ion i on the exchanger:

$$E_{\mathrm{SO4}} = \frac{2[\mathrm{A_2SO_4}]}{2[\mathrm{A_2SO_4}] + [\mathrm{ACl}]} \quad (4)$$

$$E_{\mathrm{Cl}} = \frac{[\mathrm{ACl}]}{2[\mathrm{A_2SO_4}] + [\mathrm{ACl}]} = 1 - E_{\mathrm{SO4}} \quad (5)$$

The value of the Gaines and Thomas selectivity coefficient ($K_{ex,GT}$) is related to the Rothmund and Kornfeld selectivity coefficient with:

$$K_{ex,GT} = K_{ex,RK} \left(\frac{(1 - E_{SO4})^2}{E_{SO4}} \right)^{\frac{1}{\beta}-1} \quad (6)$$

The Rothmund and Kornfeld model is equivalent to the Gaines and Thomas thermodynamic convention in the case of β=1.[21,47]

RESULTS AND DISCUSSION

Structural formula and anion exchange capacity of micro- and nano-GR samples. According to EPMA (Table S4 in supplementary data), the structural formula of micro-GR(Cl) was $[Fe^{2+}_{0.42(8)}Fe^{3+}_{0.25(4)}Co^{2+}_{0.33(4)}(OH)_2]\cdot Cl^-_{0.25(4)}\cdot mH_2O$, and that of nano-GR(Cl) was $[Fe^{2+}_{0.29(6)}Fe^{3+}_{0.20(3)}Co^{2+}_{0.51(5)}(OH)_2]\cdot Cl^-_{0.20(3)}\cdot mH_2O$ with *m* the stoichiometry for water molecules. The amounts of Fe deduced from these formulas, *i.e.* 7.97 mmol·g^{-1} for micro-GR(Cl) and 4.63 mmol·g^{-1} for nano-GR(Cl), compared well with those obtained with the 1,10-phenanthroline method (7.34 mmol·g^{-1} and 4.69 mmol·g^{-1} respectively). After exchange with SO_4^{2-}, structural formulas became $[Fe^{2+}_{0.44(4)}Fe^{3+}_{0.22(2)}Co^{2+}_{0.34(2)}(OH)_2]\cdot SO_4^{2-}{}_{0.11(1)}\cdot mH_2O$ and $[Fe^{2+}_{0.37(5)}Fe^{3+}_{0.16(2)}Co^{2+}_{0.48(3)}(OH)_2]\cdot SO_4^{2-}{}_{0.08(1)}\cdot mH_2O$ for micro-GR(SO_4) and nano-GR(SO_4) respectively. The transformation of nano-GR(Cl) and micro-GR(Cl) samples into their sulfate forms, nano-GR(SO_4) and micro-GR(SO_4) respectively, did not change significantly their layer composition, and involved a replacement of two Cl^- ions by one SO_4^{2-} ion.

TGA measurements gave similar results for the nano-GR(Cl) and the micro-GR(Cl) samples (Fig. 1 and S1to S3 in supplementary data). From room temperature to 140-150 °C, a mass loss of

~15 % was attributed to interparticle (capillary) pore water.[48] The additional ~5 % mass loss from 150 °C to 250 °C was attributed to interlayer water.[9,48–50] Mass losses were endothermic, thus supporting a water vaporization mechanism. The TGA results for nano-GR(SO_4) were similar as for nano-GR(Cl) (Fig S2). Interparticle water was evaporated between 20 and 180 °C with a mass loss of ~15 % and interlayer water from 180 to 230 °C with a mass loss of ~5 %. For micro-GR(SO_4), the first mass loss was ~10 % from 20 to 140 °C (Fig S3). The second mass loss was also 10 % from 140 °C to 310 °C. The latter temperature was much higher than the upper temperature obtained for the second mass loss of micro-GR(Cl) (240 °C). In addition, the process began to be exothermic at 140 °C, which questioned the interpretation of vaporization of interlayer water. In the following, we attributed, nonetheless, the mass loss entirely to interlayer water.

The following structural formulas were obtained with *m* calculated from Eq. (1): $Fe^{2+}_{0.42(8)}Fe^{3+}_{0.25(4)}Co^{2+}_{0.33(4)}(OH)_2]\cdot Cl^-_{0.25(4)}\cdot(H_2O)_{0.43}$ for micro-GR(Cl), $[Fe^{2+}_{0.29(6)}Fe^{3+}_{0.20(3)}Co^{2+}_{0.51(5)}(OH)_2]\cdot Cl^-_{0.20(3)}\cdot(H_2O)_{0.40}$ for nano-GR(Cl), $[Fe^{2+}_{0.44(4)}Fe^{3+}_{0.22(2)}Co^{2+}_{0.34(2)}(OH)_2]\cdot SO_4^{2-}{}_{0.11(1)}\cdot(H_2O)_{0.6}$ for micro-GR(SO_4) and $[Fe^{2+}_{0.37(5)}Fe^{3+}_{0.16(2)}Co^{2+}_{0.48(3)}(OH)_2]\cdot SO_4^{2-}{}_{0.08(1)}\cdot(H_2O)_{0.23}$ for nano-GR(SO_4). Numbers within brackets are the uncertainty on the last digit, calculated as the standard deviation of the mean value. One of the key parameters for the quantitative understanding of LDH reactivity is the determination of the anion exchange capacity that is representative of the quantity of anion that can be adsorbed by a given mass of LDH. It was first calculated from the structural formula of the fresh samples (assuming that all Cl^- was exchangeable) and that of the reacted samples (assuming that all SO_4^{2-} was exchangeable). Because of the importance of this parameter, the AEC was also calculated from the quantity of Cl^- leached by a weighted amount of green rust during the exchange with a 25 mmol·L^{-1} Na_2SO_4 solution. Although some variability was observed, all results

coherently pointed out to an AEC of two moles of electric charge per kilogram of anhydrous green rust ($mol_c \cdot kg_{anhydrous\ GR}$, Table 1).

Structure of micro- and nano-GR samples. The micro-GR(Cl) XRD pattern had numerous sharp and symmetrical peaks, which were modeled successfully with the Fougerite structure and a minor amount of magnetite (14 % - R_{wp} = 33%, R_{exp} = 8%, GoF = 17 – Fig. S4). The sole significant difference with the Fougerite model of Trolard et al.[7] was a 4-fold increase in the quantity of interlayer water, which was explained by the different hydration state of our samples during measurement. Layer symmetry was hexagonal, and could be described with a system were $a = b$ = 3.1640 Å and γ = 120°. The sole symmetrical reflection found in the nano-GR(Cl) XRD pattern were at q=0.80 and 1.59 Å and match Fougerite 00*l* reflections (Fig. S5). All other reflections were broad, most of them were asymmetrical, and their intensity was low as compared to peaks observed in micro-GR(Cl). Broadening was attributed to nanocrystallinity. However, the XRD pattern of nano-GR(Cl) was incompatible with a nanometric and 3D-ordered green rust, for which Bragg peaks would be extremely broad yet still present (Fig. S6). The asymmetrical peaks of low intensity were diagnostic for turbostratic disorder.[51,52] Indeed, the XRD pattern of turbostratic structure only contain 00*l* reflections and unsolved *hk* bands.[52] In turbostratic layered Mn oxides, which have a layer structure very close to green rust and an XRD pattern that is very similar to that observed here for nano-GR(Cl), two layer symmetries have been described. The first one is the hexagonal symmetry that can be described equally with $a = b$ and γ = 120 ° or with the equivalent $a = \sqrt{3} \times b$, γ = 90 ° system (Fig S7), and the second one is the orthogonal layer symmetry ($a > \sqrt{3} \times b$ and γ = 90 °).[53]. Hexagonal and orthogonal layer symmetries can be distinguished from the ratio of the *d*-spacing of the 11,20 and 31,02 bands (using an indexing with

296 $\gamma = 90$ °) and the shape of the 31,02 band: in the hexagonal layer symmetry, it is equal to √3, and
297 the 31,02 band is almost symmetrical. In this study, the ratio of the *d*-spacing of the two bands at
298 $q = 2.34$ Å^{-1} and ~4.03 Å^{-1}, assigned to be the 11,20 and 31,02 bands, respectively, was 1.72, close
299 to √3. Consequently, nano-GR had, like micro-GR, hexagonal layer symmetry.[36,53,54] This
300 observation reinforced the hypothesis of nano-GR(Cl) being a nanometric and turbostratic
301 variation of micro-GR(Cl).

302 Despite the distinctive shapes of micro-GR(Cl) and nano-GR(Cl) XRD patterns, the PDF of both
303 samples were overlaid for *r* values lower than 5.95 Å, which corresponds to the layer-to-layer
304 distance of a green rust containing interlayer Cl^- (7.95 Å) minus the layer thickness (2 Å, Fig. 2A).
305 Because the area of a PDF correlation is directly proportional to the number of atoms involved in
306 the correlation and to their nature,[40] this overlay at low *r* values indicated that nano- and micro-
307 GR(Cl) had the same layer structure, and further supported the hypothesis of nano-GR(Cl) being
308 a disordered (turbostratic) variation of micro-GR(Cl). At *r* values higher than 5.95 Å, several
309 correlations that were present in the PDF of the micro-GR(Cl) sample were absent in the PDF of
310 the nano-GR(Cl) sample. The same correlations were present in the calculated Fougerite PDF,
311 whereas they were absent in the calculated PDF of a single Fougerite sheet (Fig. 2B). Calculation
312 of a partial PDF showed that these missing correlations were attributable to Me-Me atomic pairs
313 (Fig. 2A, Me = $Fe^{2+,3+}$, Co^{2+}) with the two atoms being located in distinct layers, because they
314 were absent in the calculated PDF of a single Fougerite layer (Fig. 2C). In contrast, the Me-Me
315 pairs that were observed in the two calculated PDF (e.g., at 8.02, 12.25, 12.1-12.3, and 15 Å – Fig.
316 2A), and that could thus be attributed to Me-Me atomic pairs within a given layer, were also
317 observed in the experimental PDF of both nano-GR(Cl) and micro-GR(Cl). Finally, the Me-Me
318 correlations gradually shifted towards low *r* values with increasing *r* in the PDF of nano-GR(Cl)

relative to those of micro-GR(Cl). Consequently, the in-plane lattice parameters of nano-GR(Cl) were slightly smaller than those of micro-GR(Cl). Nano-GR(Cl) layers had a higher Co^{2+}/Fe^{2+} ratio than micro-GR(Cl), and the ionic radius of Co^{2+} is ~5 % smaller than that of Fe^{2+} in octahedral coordination.[55] Thus, the smaller values of in-plane lattice parameters for nano-GR(Cl) compared to micro-GR(Cl) were consistent with this difference in layer composition. The PDF of nano-GR(Cl) canceled at r ~50 Å, whereas several intense correlations were present at higher r values in the PDF of micro-GR(Cl), consistent with nano-GR(Cl) being nanocrystalline, and micro-GR(Cl) being microcrystalline. Such hypothesis was confirmed by a Fourier transform of the $r >$ 50 Å part of the PDF, where no signal attributable to the sample could be detected for nano-GR(Cl) (data not shown). PDF results were thus in agreement with our interpretation of XRD data.

TEM images evidenced two distinct morphologies for nano-GR(Cl) and micro-GR(Cl) (Fig.Figure 3). Nano-GR(Cl) crystals were systematically aggregated and xenomorphic. Micro-GR(Cl) crystals were automorphic and their size in the **a-b** plane varied between 0.1 and 1 µm with a maximum thickness along **c*** of 40 nm. Thus, only the morphology of micro-GR(Cl) could be determined with confidence. Layer-to-layer distances, deduced from a Fast Fourier transform () analysis of the images, were: 7.1 Å for nano-GR(Cl) and 7.4 Å for micro-GR(Cl). Those values were lower than the layer-to-layer distances deduced from XRD analysis due to TEM conditions.

Mechanism of transformation from GR(Cl) to GR(SO_4). Na_2SO_4 and NaCl solution was flowed through nano- and micro-GR(Cl), thus transforming them to GR(SO_4). During this exchange, the intensity of the X-ray reflection at q = 0.78 $Å^{-1}$ (equivalent to a d-spacing of 7.95 Å) steadily decreased with time, while a reflection appeared and increased in intensity at 0.57 $Å^{-1}$ (d = 11.02 Å; Fig. 4). Concomitantly, almost all peaks present at higher q values in the XRD

pattern of micro-GR also shifted, with the noticeable exception of those having *hk*0 indices (e.g., the 110 reflection at q = 3.89 Å^{-1}). This was most straightforwardly explained by an increase in *c* during the experiment, while *a* and *b* remained unaffected. For nano-GR, only 00*l* reflections were shifting. At higher q values, the position of all *hk* bands remained unchanged, consistent with *c* increasing and *a* and *b* remaining constant. However, the shape of the high-q side of the 11,20 band at 2.34 Å^{-1} evolved. This was due to a change in the nature, location and (or) density of the atoms in the lattice,[52] consistent with an anion exchange.

The increase in *c* in both samples was consistent with the replacement of Cl^- by SO_4^{2-} in the interlayer. The 00*l* reflections of nano- and micro-GR(Cl) and of nano- and micro-GR(SO_4) remained symmetrical and did not exhibit significant width changes during the experiment. In addition, every reflection of *hkl* indices with $l \neq 0$ changed from the position corresponding to the Cl^- variation to the position corresponding to the SO_4^{2-} variation without a gradual shift and without the appearance of a peak at an intermediate position. Finally, the average crystallite size remained constant throughout the experiments (Figs. 4D). Collectively, these observations showed that a simple anion exchange mechanism occurred without dissolution-recrystallization processes, and that an interstratification phenomenon (*i.e.* ordered or disordered alternations of Cl^- and SO_4^{2-} interlayers within a given crystal) was also unlikely.[51]

Cation exchange selectivity coefficient. Cl^- – SO_4^{2-} exchange data could not be modeled with an ion exchange model using a constant selectivity coefficient and using the usual exchange conventions of Vanselow, Gaines and Thomas, or Gapon.[21,56] With these ion exchange conventions, it was necessary to increase the value of the selectivity coefficient with an increase of SO_4^{2-} occupancy in the exchanger. Such changes of selectivity coefficient values as a function

of chemical conditions are usually well captured with a Rothmund and Kornfeld model (Eq. (3)).[21,47] Indeed, an acceptable fit of the data was obtained with a $\log_{10} K_{ex,RK}$ value of 0.3 and a β value of 2.4 for the micro-GR sample (Fig. 5), and with a $\log_{10} K_{ex,RK}$ value of 0.2 and a β value of 5 for the nano-GR sample (Fig. 6). The model predicted that 86 % and 95 % of the exchange sites were occupied by SO_4^{2-} in the micro-GR and nano-GR samples respectively, at equilibrium with an aqueous solution containing 40 mmol·L^{-1} $Cl^-$and 5 mmol·L^{-1} SO_4^{2-}. These results were in agreement with XRD data that showed that Cl^- interlayers were only a minor component after equilibration of the sample with this aqueous solution (Fig. 4).

The values of β were larger than one, meaning that the Gaines and Thomas selectivity coefficient $K_{ex,GT}$ of the $Cl^- \rightarrow SO_4^{2-}$ exchange reaction increased with the SO_4^{2-}occupancy on the exchanger. A large increase of the A→B selectivity coefficient with an increase of the exchanger occupancy by species B is at variance with observations made on cationic clays for which the reverse tendency has been observed frequently. The decrease of the selectivity in clays is usually linked to the presence of several types of adsorption sites with decreasing affinities for the species B compared to species A.[57–61] Consequently, the mechanism of anion exchange in green rust interlayers may be different from ion exchange in cationic clay minerals interlayers. Miyata observed also a monotonous increase of the $NO_3^- \rightarrow Br^-$ selectivity coefficient with the Br^- exchanger occupancy on Mg-Al hydrotalcite-like compounds (Mg-Al LDH).[62] Because of the similarities of structure between Mg-Al LDH and green rust, we speculate that the peculiar anion exchange properties of green rust could be related to the structuration of anions in the interlayer, which is influenced by the geometry of the anion (spherical and point charge for Cl^-, tetrahedral oxyanion for sulfate), the high charge density (0.18 C.m^{-2} for micro-GR compared to -0.11 C.m^{-2} for Wyoming montmorillonite) and the high surface occupation.[20,63]

Environmental implications. The importance of anion adsorption in by LDH in general, and green rust in particular, has been highlighted in many studies.[2,10,26,29,31,64–69] It is also usually acknowledged that the affinity of the interlayer adsorption sites varies as a function of inorganic anions (*e.g.* Cl^-, NO_3^-, SO_4^{2-}, F^-, HCO_3^-/CO_3^{2-}), but this comes mostly from analogy with the properties of LDH compounds.[2,15,26,70] It is thus surprising that so few thermodynamic evaluations of the affinity of interlayer sites for anions were attempted.[2,15] It is even more surprising that the ion exchange theory was not applied to model LDH reactivity in general and green rust in particular, when considering that LDH are commonly presented as the anionic versions of cationic clays,[71] the natural material for which the ion exchange theory has been the most developed and applied. In this study, the information gathered from time-resolved diffractometric data, TGA and bulk chemistry provided solid evidences that an anion exchange mechanism takes place in green rust interlayers without significant structural changes other than interlayer swelling. We found that the affinity of green rust for SO_4^{2-} compared to Cl^- increased with increasing SO_4^{2-} occupancy of the surface sites. This property can be reproduced with a Rothmund and Kornfeld exchange model. Additional experiments with other couples of competing ions and with other green rust samples with a range of substituted cations are now necessary to confirm the suitability of the Rothmund and Kornfeld exchange model to reproduce anion exchange data. Those studies would help to build an anion exchange database for the modeling and prediction of anion adsorption in green rusts present in hydromorphic soils (Fougerite) and engineered settings.

408 FIGURES (Word Style “VA_Figure_Caption”).

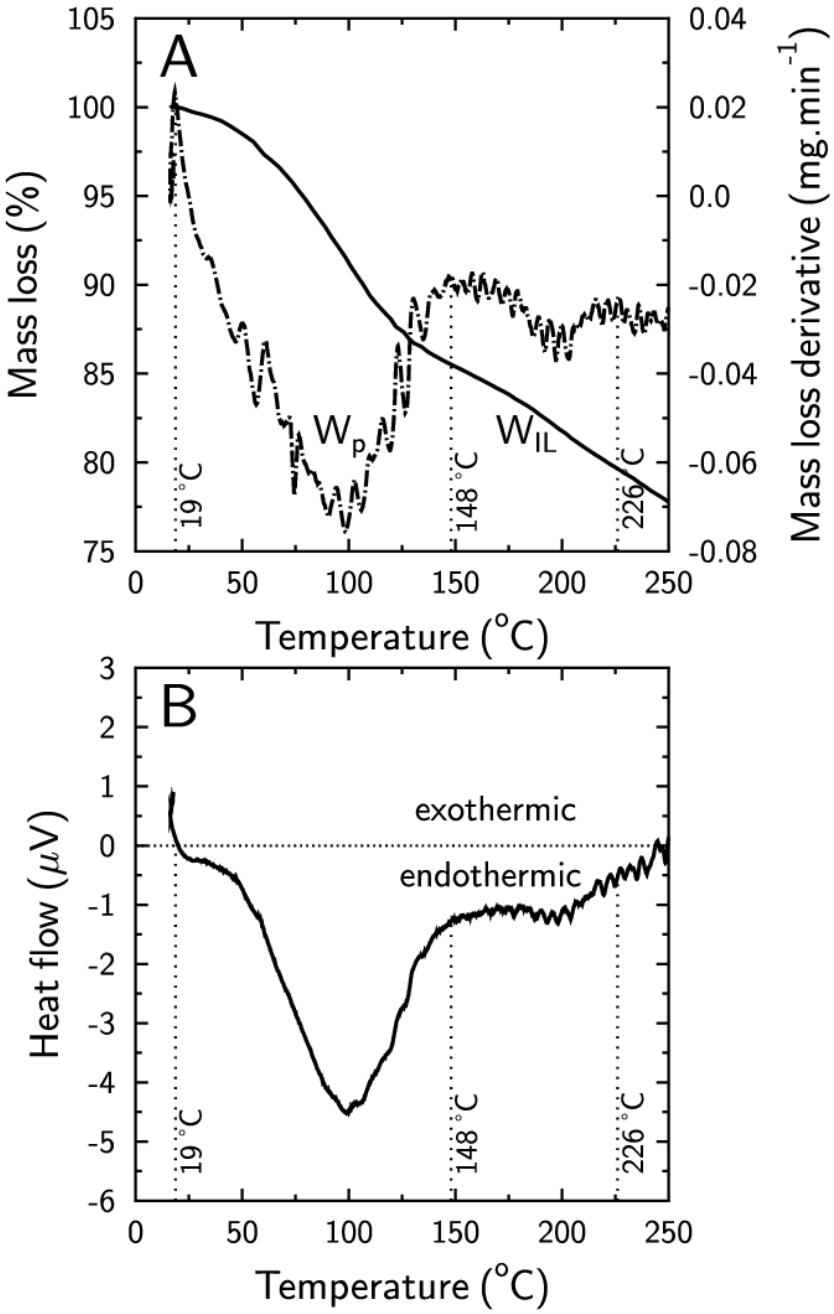

409

410 Figure 1. A: TGA results for nano-GR(Cl). Full line: mass loss (%); Dash line: mass loss derivative

411 (mg·min^{-1}); W_P= interparticle (capillary) pore water; W_{IL}= interlayer water. B: DSC results.

412

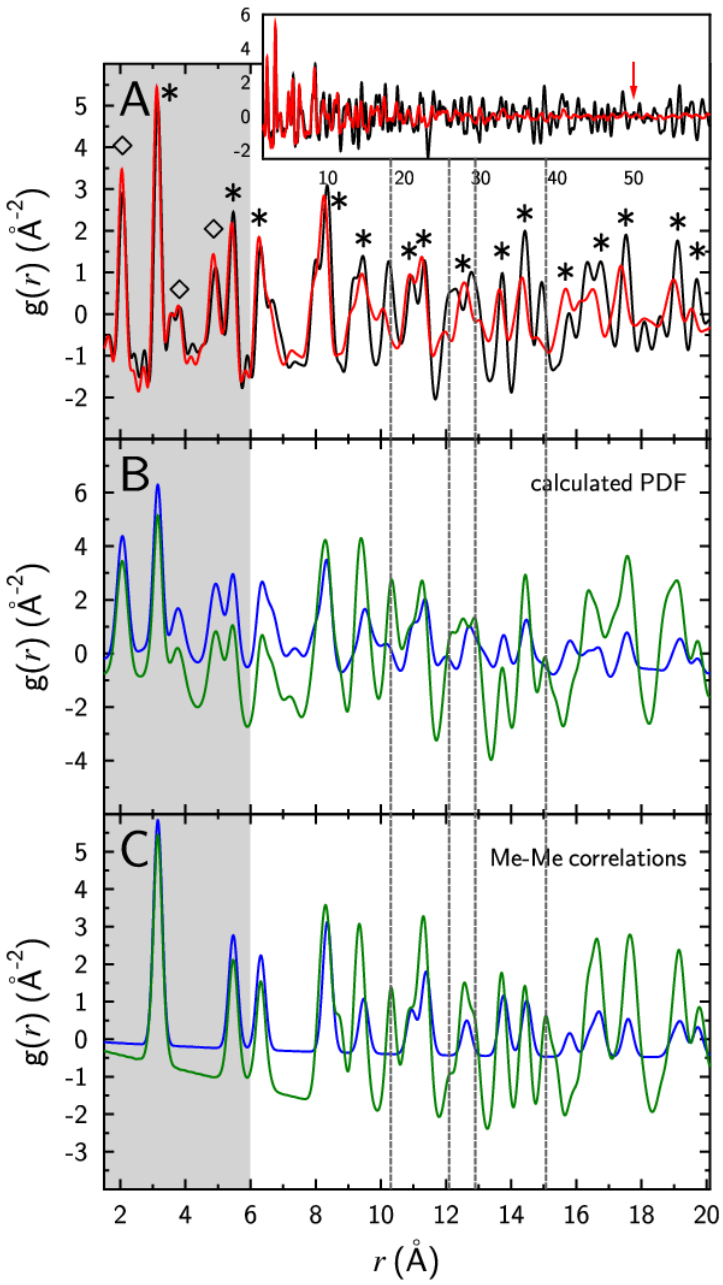

413

414 Figure 2: A: PDF data of nano-GR(Cl) (red solid line) and micro-GR(Cl) (black solid line). Inset:
415 data up to r = 60 Å, with the arrow pointing out to the r value at which the PDF from nano-GR(Cl)
416 is below periodic noise. Main panel: detail of the 1.5-20 Å region, with indexation of the main
417 correlations. Me-Me = $Fe^{2+,3+}$ — $Fe^{2+,3+}$, $Fe^{2+,3+}$ — Co^{2+} or Co^{2+} — Co^{2+} correlations (indicated
418 by a star). Me-O= $Fe^{2+,3+}$— O or Co^{2+}— O correlations (indicated by a diamond). B: calculated

PDF for a Fougerite[7] (green solid line) and for a single Fougerite layer (blue solid line). See main text for details concerning the calculation. C: partial PDF showing only the Me-Me correlations for a Fougerite (green solid line) and a single Fougerite layer (blue solid line). The grey-shaded area corresponds to *r* values lower than the Me to Me distance in adjacent layers. No data normalization.

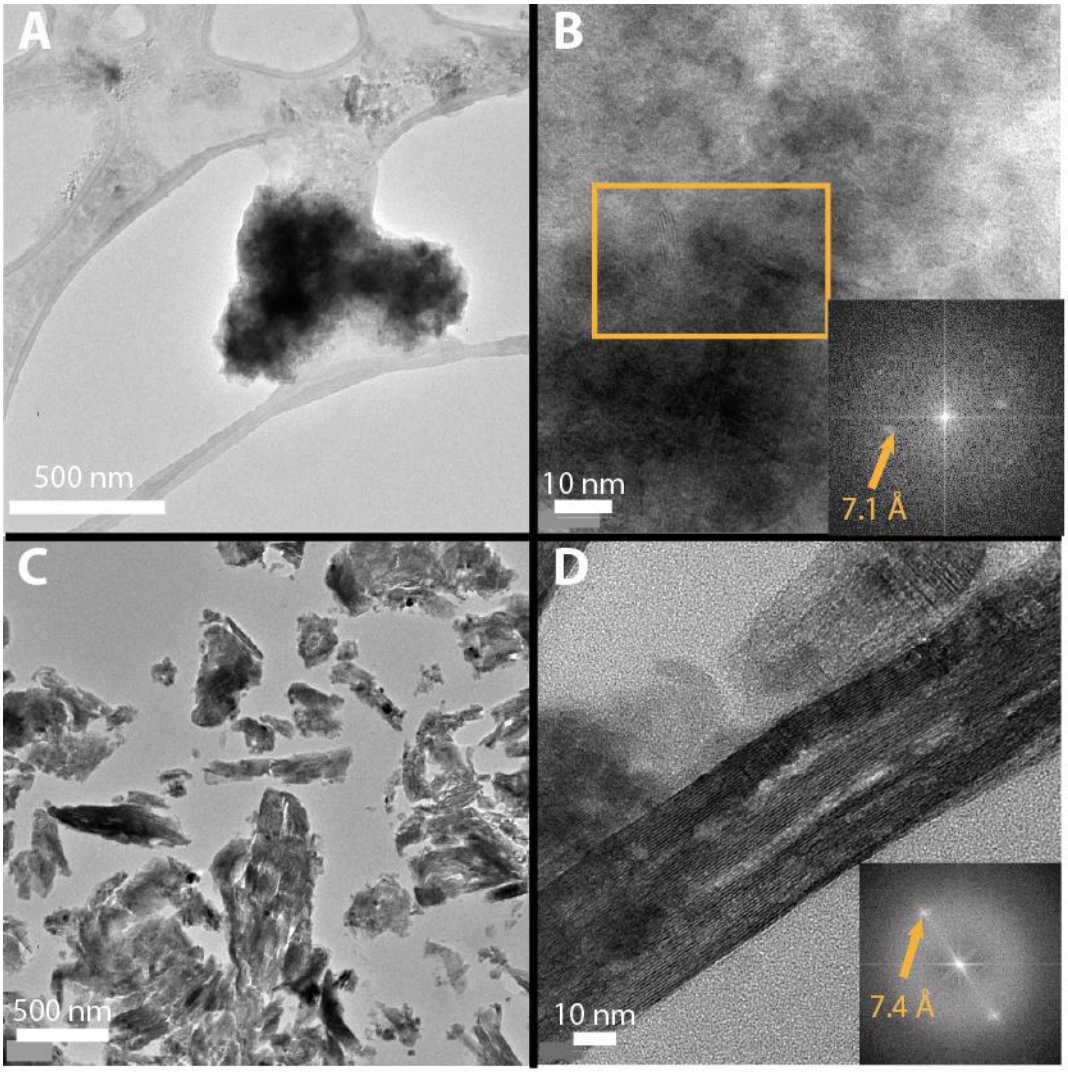

424

425 Figure 3. TEM images of nano-GR(Cl) (A, B) and micro-GR(Cl) (C, D). Insert in B: FFT of the
426 area described by the orange box in B. Insert in C: FFT analysis of the whole TEM images in D.

427

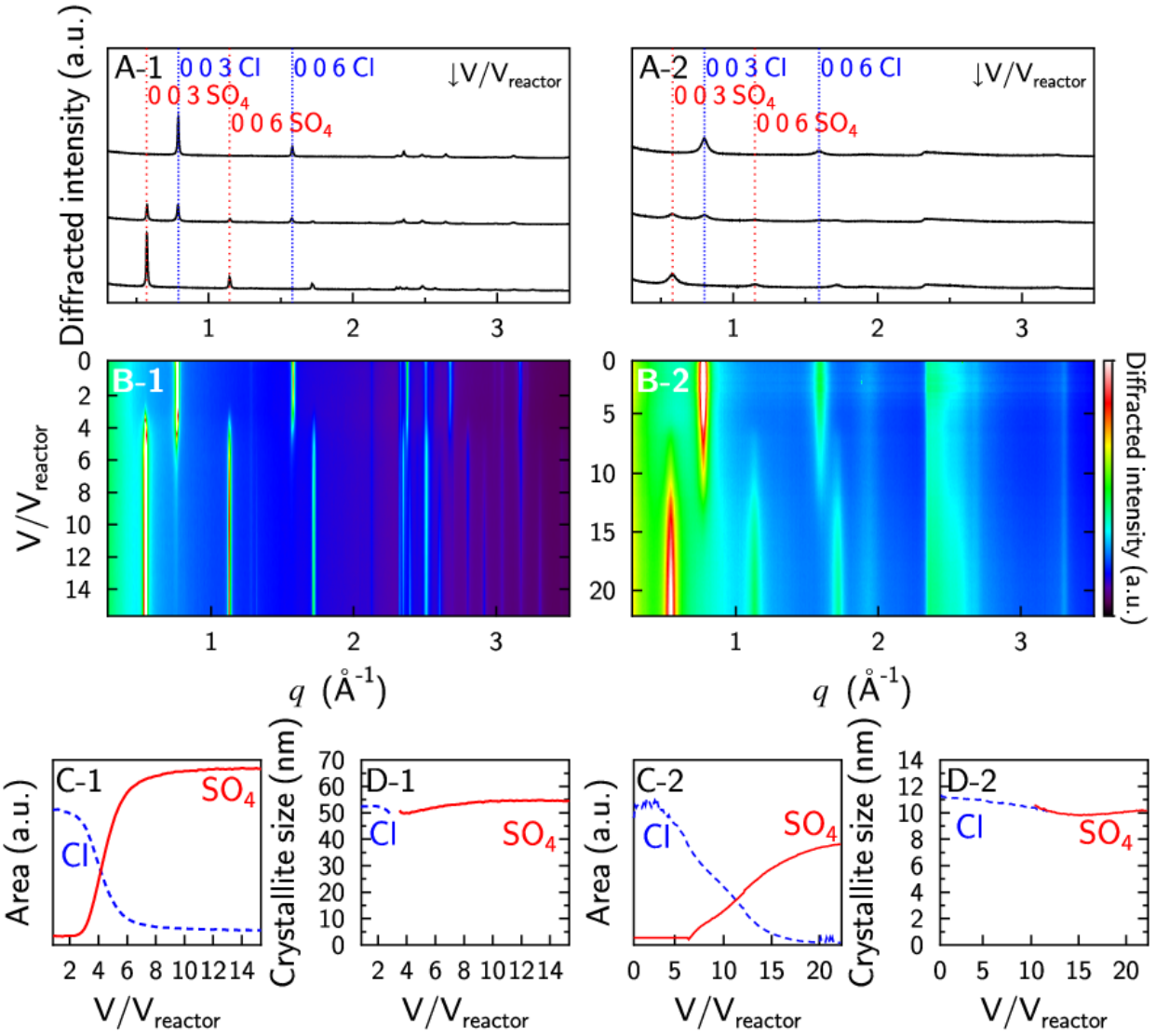

Figure 4. XRD patterns recorded in-situ during the 5 mmol·L^{-1} Na_2SO_4 / 40 mmol·L^{-1} NaCl solution flow-through experiment with micro-GR(Cl) (left - 1) and nano-GR(Cl) (right - 2) . A-1: patterns recorder after 2, 4 and 14 pore volumes ($V/V_{reactor}$). A-2: patterns recorder after 0, 10 and 20 $V/V_{reactor}$. B: 2D map of XRD patterns as a function time expressed in pore volumes. C: Evolution of the 003 peak areas at 0.78 Å (Cl^- interlayer, blue dash line) and 0.57 Å (SO_4^{2-} interlayer, red line) as a function of pore volumes. D: Estimate of the crystallite size as a function of time inferred from full width at half maximum of the 003 peak and Scherrer equation at 0.78 Å

436 (Cl^- interlayer, blue dash line) and 0.57 Å (SO_4^{2-} interlayer, red line) . Note: the same peak indexing

437 formalism was followed for nano-GR despite the lack of a 3D-ordered structure.

438

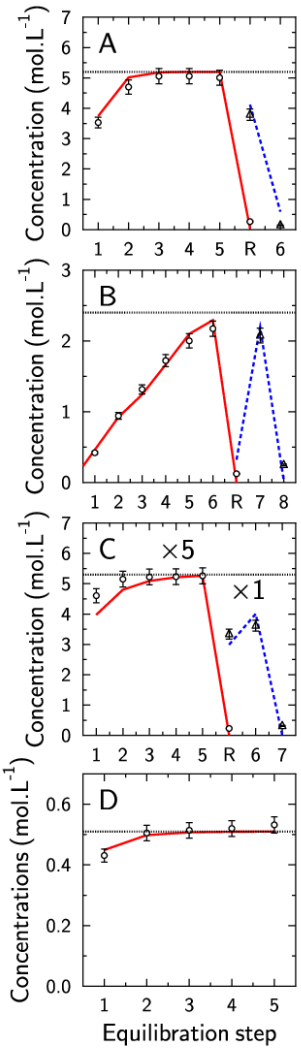

Figure 5. SO_4^{2-}/Cl^- exchange data on micro-GR (SO_4^{2-}: circles; Cl^-: triangles). The initial sample was saturated with Cl^-. Steps 1 to 5 (or 6 on figure B) correspond to equilibration with Na_2SO_4/NaCl solutions with total Na concentration of 50 mmol·L^{-1}. The black dash lines represent the SO_4^{2-} input concentration (the SO_4^{2-} concentration values are multiplied by 5 on figure B). Step R corresponds to the rinsing of the sample with ultrapure water. Steps 6 and 8 correspond to equilibration steps with 25 mmol·L^{-1} of Na_2SO_4 (or 7 and 8 on figure B). Red and blue lines represent the results of the Rothmund and Kornfeld exchange model with $\log_{10} K_{ex,RK}$ =0.3 and β=2.4. SO_4^{2-} concentrations and blue dashed line is Cl^- concentrations given by the model. The AEC value was taken at 2 mol_c·kg^{-1}.

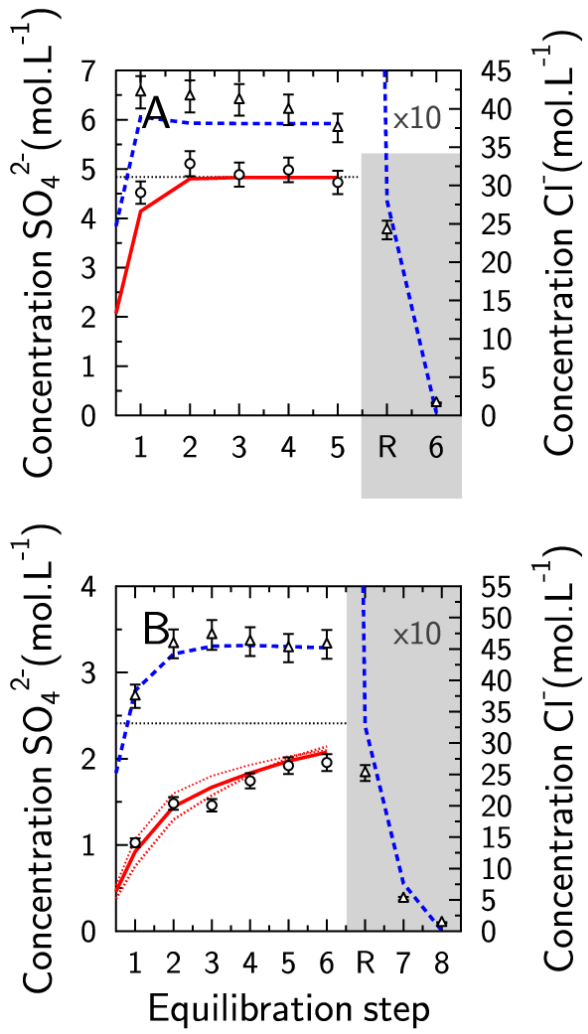

Figure 6. SO_4^{2-}/Cl^- exchange data on nano-GR (SO_4^{2-}: circles; Cl^-: triangles). The initial sample was saturated with Cl^-. Steps 1 to 5 (or 6 on figure B) correspond to equilibration with Na_2SO_4/NaCl solutions with total Na concentration of 50 mmol·L^{-1}. The black dash lines represent the SO_4^{2-} input concentration. Step R corresponds to the rinsing of the sample with ultrapure water. Steps 6 and 8 correspond to equilibration steps with 25 mmol·L^{-1} of Na_2SO_4 (or 7 and 8 on figure B). Colored lines represent the results of the Rothmund and Kornfeld exchange model with $\log_{10} K_{ex,RK}$ = 0.2 and β=5. The red dotted lines are SO_4^{2-} concentrations from the same model but with β=3 and β=7 ($\log_{10} K_{ex,RK}$ = 0.2). The AEC value was taken at 1.6 mol$_c$·kg^{-1}.Concentrations of Cl^- from measurements and model are multiplied by 10 in the grey area.

459 TABLES.

460 Table 1. Anion exchange capacity (AEC in $mol_c/kg_{anhydrous\ GR}$) of nano- and micro-GR samples,
461 according to three characterization methods.

Sample	AEC EPMA (Cl^-)	AEC EPMA (SO_4^{2-})	AEC Exchange Na_2SO_4
nano-GR	2 ± 0.2	1.8 ± 0.2	1.62 ± 0.2
micro-GR	2.5 ± 0.2	2 ± 0.3	2.0 ± 0.3

462

463

AUTHOR INFORMATION

Corresponding Author

*myriam.agnel@cnrs-orleans.fr -1A Rue de la Ferollerie, 45071 Orléans – +33 (0) 2 38 64 30 85 – https://orcid.org/0000-0001-5027-6257

Author Contributions

M.A., S.G., and C.T. conceived and designed the exchange experiments. M.A. conducted green rust synthesis and batch exchange experiments. M.A., S.G., F.F., E.E., F.C. and C.T. conducted the synchrotron experiments. F.F., E.E., F.C., M.R. and F.W. contributed materials and analysis tools. M.A., S.G., and C.T. analyzed the data and co-wrote the paper.

ACKNOWLEDGMENTS

The authors thank Guillaume Wille and Mollud Alleki for assistance with EPMA sample preparation and measurements. S. Grangeon acknowledges funding from the ANR (NACRE—ANR-14-CE01-0006) and Julie Philibert for fruitful discussions. M.I. Agnel acknowledges funding for her PhD from the Région Centre-Val de Loire and Clément Jauvion for constructive discussions. The authors thank the three anonymous reviewer and Prof. Daniel Giammar for their comments and suggestions.

SOLEIL and ALBA data were acquired in the frame of proposals 20170391 and 2017022082, respectively.

SUPPORTING INFORMATION AVAILABLE.

SI_GR_Agnel.pdf (format PDF) – his information is available free of charge via the Internet at http://pubs.acs.org. A file containing the Scherrer equation, TGA results, experimental and

485 calculated XRD patterns, results of Rietveld refinement on micro-GR(Cl) and tables with anion
486 exchange experiments data and microprobe results. The main article can be read without this
487 information.

488

489 ABBREVIATIONS

490 GR, green rust; LDH, layered double hydroxide; CoHex, hexamminecobalt(III) chloride; EPMA,
491 electron probe micro-analyzes; TGA, thermogravimetric analyses; DTA, differential thermal
492 analysis; XRD, X-ray diffraction; PDF, X-ray Pair Distribution Function; AEC, anion exchange
493 capacity; FFT, Fast Fourier transform.

494 REFERENCES

495 (1) Trolard, F.; Bourrié, G. Chapter 5 - Geochemistry of green rusts and Fougerite: A
496 reevaluation of Fe cycle in soils; In *Adv. Agron.*; Academic Press, 2008; Vol. 99, pp. 227–
497 288.
498 (2) Usman, M.; Byrne, J. M.; Chaudhary, A.; Orsetti, S.; Hanna, K.; Ruby, C.; Kappler, A.;
499 Haderlein, S. B. Magnetite and green Rust: Synthesis, properties, and environmental
500 applications of mixed-valent iron minerals. *Chem. Rev.* **2018**, *118*, 3251–3304.
501 (3) Vodyanitskii, Y. N.; Shoba, S. A. Ephemeral Fe(II)/Fe(III) layered double hydroxides in
502 hydromorphic soils: A review. *Eurasian Soil Sci.* **2015**, *48*, 240–249.
503 (4) Abdelmoula, M.; Trolard, F.; Bourrié, G.; Génin, J.-M. R. Evidence for the Fe(II)-Fe(III)
504 green rust "Fougerite" mineral occurence in hydromorphic soil and its transformation with
505 depth. *Hyperfine Interact.* **1998**, *112*, 235–238.
506 (5) Trolard, F.; Abdelmoula, M.; Bourrié, G.; Humbert, B.; Génin, J.-M. R. Mise en évidence
507 d'un constituant de type «rouilles vertes» dans les sols hydromorphes. Proposition de
508 l'existence d'un nouveau minéral : la «fougérite». *Comptes rendus de l'Académie des*
509 *sciences. Série 2. Sciences de la terre et des planètes* **1996**, *323*, 1015–1022.
510 (6) Trolard, F.; Génin, J.-M. R.; Abdelmoula, M.; Bourrié, G.; Humbert, B.; Herbillon, A.
511 Identification of a green rust mineral in a reductomorphic soil by Mossbauer and Raman
512 spectroscopies. *Geochim. Cosmochim. Acta* **1997**, *61*, 1107–1111.
513 (7) Trolard, F.; Bourrié, G.; Abdelmoula, M.; Refait, P.; Feder, F. Fougerite, a new mineral of
514 the pyroaurite-iowaite group: Description and crystal structure. *Clays Clay Miner.* **2007**,
515 *55*, 323–334.
516 (8) Christiansen, B. C.; Balic-Zunic, T.; Dideriksen, K.; Stipp, S. L. S. Identification of green
517 rust in groundwater. *Environ. Sci. Technol.* **2009**, *43*, 3436–3441.
518 (9) Hansen, H. C. B.; Kock, C. B.; Nancke-Krogh, H.; Borggaard, O. K.; Sorensen, J. Abiotic
519 nitrate reduction to ammonium: Key role of green rust. *Environ. Sci. Technol.* **1996**, *30*,
520 2053–2056.
521 (10) Holmes, A. B.; Gu, F. X. Emerging nanomaterials for the application of selenium removal
522 for wastewater treatment. *Environ. Sci.: Nano* **2016**, *3*, 982–996.
523 (11) O'Loughlin, E. J.; Kelly, S. D.; Cook, R. E.; Csencsits, R.; Kemner, K. M. Reduction of
524 Uranium(VI) by mixed Iron(II)/Iron(III) hydroxide (green rust): Formation of UO2
525 nanoparticles. *Environ. Sci. Technol.* **2003**, *37*, 721–727.
526 (12) Su, C. Environmental implications and applications of engineered nanoscale magnetite and
527 its hybrid nanocomposites: A review of recent literature. *J. Hazard. Mater.* **2017**, *322*, 48–
528 84.
529 (13) Zegeye, A.; Bonneville, S.; Benning, L. G.; Sturm, A.; Fowle, D. A.; Jones, C.; Canfield,
530 D. E.; Ruby, C.; MacLean, L. C.; Nomosatryo, S.; Crowe, S. A.; Poulton, S. W. Green rust
531 formation controls nutrient availability in a ferruginous water column. *Geology* **2012**, *40*,
532 599–602.
533 (14) Bhave, C.; Shejwalkar, S. A review on the synthesis and applications of green rust for
534 environmental pollutant remediation. *Int. J. Environ. Sci. Technol.* **2018**, *15*, 1243–1248.
535 (15) Rives, V. *Layered double hydroxides: Present and future*; Nova Science Publishers Inc.,
536 2001; pp. 1–495.
537 (16) Sumoondur, A.; Shaw, S.; Ahmed, I.; Benning, L. G. Green rust as a precursor for
538 magnetite: an in situ synchrotron based study. *Mineral. Mag.* **2008**, *72*, 201–204.

(17) He, Y. T.; Wilson, J. T.; Su, C.; Wilkin, R. T. Review of abiotic degradation of chlorinated solvents by reactive iron minerals in aquifers. *Groundwater Monit. Rem.* **2015**, *35*, 57–75.
(18) Refait, P.; Génin, J. M. R. The oxidation of ferrous hydroxide in chloride-containing aqueous media and pourbaix diagrams of green rust one. *Corros. Sci.* **1993**, *34*, 797–819.
(19) Cornell, R. M.; Schwertmann, U. Chapter 13 - Green Rusts; In *Iron Oxides in the Laboratory: Preparation and Characterization*; John Wiley & Sons, 2008; pp. 143–145.
(20) Génin, J. M. R.; Abdelmoula, M.; Ruby, C.; Upadhyay, C. Speciation of iron; characterisation and structure of green rusts and FeII-IIIoxyhydroxycarbonate fougerite. *C. R. Geosci.* **2006**, *338*, 402–419.
(21) Sposito, G. *The thermodynamics of soil solution*; Oxford University Press, 1981; p. 231.
(22) Peacock, C. L.; Sherman, D. M. Sorption of Ni by birnessite: Equilibrium controls on Ni in seawater. *Chem. Geol.* **2007**, *238*, 94–106.
(23) Refait, P.; Géhin, A.; Abdelmoula, M.; Génin, J.-M. R. Coprecipitation thermodynamics of iron(II–III) hydroxysulphate green rust from Fe(II) and Fe(III) salts. *Corros. Sci.* **2003**, *45*, 659–679.
(24) Sparks, D. L. Elucidating the fundamental chemistry of soils: Past and recent achievements and future frontiers. *Geoderma* **2001**, *100*, 303–319.
(25) Refait, P.; Génin, J.-M. . The transformation of chloride-containing green rust one into sulphated green rust two by oxidation in mixed Cl^- and SO_4^{2-} aqueous media. *Corros. Sci.* **1994**, *36*, 55–65.
(26) Trolard, F. Fougerite: From field experiment to the homologation of the mineral. *C.R. Geosci.* **2006**, *338*, 1158–1166.
(27) Fan, G.; Li, F.; Evans, D. G.; Duan, X. Catalytic applications of layered double hydroxides: recent advances and perspectives. *Chem. Soc. Rev. Chem. Soc. Rev* **2014**, *7040*, 7040–7066.
(28) Marty, N. C. M.; Grangeon, S.; Elkaïm, E.; Tournassat, C.; Fauchet, C.; Claret, F. Thermodynamic and crystallographic model for anion uptake by hydrated calcium aluminate (AFm): an example of molybdenum. *Sci. Rep.* **2018**, *8*, 7943.
(29) Barthélémy, K.; Naille, S.; Despas, C.; Ruby, C.; Mallet, M. Carbonated ferric green rust as a new material for efficient phosphate removal. *J. Colloid Interface Sci.* **2012**, *384*, 121–127.
(30) Caraballo, M. A.; Michel, F. M.; Hochella, M. F. The rapid expansion of environmental mineralogy in unconventional ways: Beyond the accepted definition of a mineral, the latest technology, and using nature as our guide. *Am. Mineral.* **2015**, *100*, 14–25.
(31) Johnson, C. A.; Murayama, M.; Küsel, K.; Hochella, M. F. Polycrystallinity of green rust minerals and their synthetic analogs: Implications for particle formation and reactivity in complex systems. *Am. Mineral.* **2015**, *100*, 2091–2105.
(32) Hadi, J.; Grangeon, S.; Warmont, F.; Seron, A.; Greneche, J. M. A novel and easy chemical-clock synthesis of nanocrystalline iron-cobalt bearing layered double hydroxides. *J. Colloid Interface Sci.* **2014**, *434*, 130–140.
(33) Johnson, C. A.; Freyer, G.; Fabisch, M.; Caraballo, M. A.; Küsel, K.; Hochella, M. F. Observations and assessment of iron oxide and green rust nanoparticles in metal-polluted mine drainage within a steep redox gradient. *Environ. Chem.* **2014**, *11*, 377–391.
(34) Fauth, F.; Boer, R.; Gil-Ortiz, F.; Popescu, C.; Vallcorba, O.; Peral, I.; Fullà, D.; Benach, J.; Juanhuix, J. The crystallography stations at the Alba synchrotron. *Eur. Phys. J. Plus* **2015**, *130*, 160.

(35) Fauth, F.; Peral, I.; Popescu, C.; Knapp, M. The new Material Science Powder Diffraction beamline at ALBA Synchrotron. *Powder Diffr.* **2013**, *28*, S360–S370.
(36) Grangeon, S.; Fernandez-Martinez, A.; Claret, F.; Marty, N.; Tournassat, C.; Warmont, F.; Gloter, A. In-situ determination of the kinetics and mechanisms of nickel adsorption by nanocrystalline vernadite. *Chem. Geol.* **2017**, *459*, 24–31.
(37) Muniz, F. T.; Aurélio, M.; Miranda, R.; Morilla, C.; Santos, D.; Sasaki, J. M. The Scherrer equation and the dynamical theory of X-ray diffraction. *Acta Crystallogr., Sect. A: Found. Adv.* **2016**, *72*, 385–390.
(38) Rodríguez-Carvajal, J. Recent advances in magnetic structure determination by neutron powder diffraction. *Physica B* **1993**, *192*, 55–69.
(39) Wechsler, B. A.; Lindsley, D. H.; Prewitt, C. T. Crystal structure and cation distribution in titanomagnetites ($Fe_{(3-x)}Ti_xO_4$). *Am. Mineral.* **1984**, *69*, 754–770.
(40) Egami, T.; Billinge, S. J. L. Chapter 3 The method of total scattering and atomic pair distribution function analysis; In *Underneath the Bragg peaks : structural analysis of complex materials*; Pergamon, 2012; Vol. 16, pp. 55–99.
(41) Grangeon, S.; Fernandez-Martinez, A.; Baronnet, A.; Marty, N.; Poulain, A.; Elkaïm, E.; Roosz, C.; Gaboreau, S.; Henocq, P.; Claret, F. Quantitative X-ray pair distribution function analysis of nanocrystalline calcium silicate hydrates: a contribution to the understanding of cement chemistry. *J. Appl. Cryst* **2017**, *50*, 14–21.
(42) Ounsy, M.; Girardot, R.; Saintin, K.; Viguier, G. Online data reduction for high throughput beamlines; In *ICALEPCS*; 2013; p. 217.
(43) Juhás, P.; Davis, T.; Farrow, C. L.; Billinge, S. J. L. PDFgetX3 : a rapid and highly automatable program for processing powder diffraction data into total scattering pair distribution functions. *J. Appl. Cryst* **2013**, *46*, 560–566.
(44) Zhu, M.; Farrow, C. L.; Post, J. E.; Livi, K. J. T.; Billinge, S. J. L.; Ginder-Vogel, M.; Sparks, D. L. Structural study of biotic and abiotic poorly-crystalline manganese oxides using atomic pair distribution function analysis. *Geochim. Cosmochim. Acta* **2012**, *81*, 39–55.
(45) Shi, C.; Beidaghi, M.; Naguib, M.; Mashtalir, O.; Gogotsi, Y.; Billinge, S. J. L. Structure of nanocrystalline Ti_3C_2 MXene using atomic pair distribution function. *Phys. Rev. Lett.* **2014**, *112*,.
(46) Parkhurst, D. L.; Appelo, C. A. J. *Description of input and examples for PHREEQC version 3—A computer program for speciation, batch-reaction, one-dimensional transport, and inverse geochemical calculations*; U.S. Geological Survey Techniques and Methods, 2013; p. 497.
(47) Bond, W. J. On the Rothmund-Kornfeld description of cation exchange. *Soil Sci. Soc. Am. J.* **1995**, *59*, 436–443.
(48) Yun, S. K.; Pinnavaia, T. J. Water content and particle texture of synthetic Hydrotalcite-like layered double hydroxides. *Chem. Mater.* **1995**, *7*, 348–354.
(49) Miyata, S.; Okada, A. Synthesis of Hydrotalcite-like compounds and their physico-chemical properties - the systems Mg^{2+}-Al^{3+}-SO_4^{2-} and Mg^{2+}-Al^{3+}-CrO_4^{2-} . *Clays Clay Miner.* **1977**, *25*, 14–18.
(50) Palmer, S. J.; Frost, R. L.; Nguyen, T. Thermal decomposition of hydrotalcite with molybdate and vanadate anions in the interlayer. *J. Therm. Anal. Calorim.* **2008**, *92*, 879–886.

(51) Drits, V. A.; Tchoubar, C. *X-ray diffraction by disordered lamellar structures*; Springer-Verlag, 1990; p. 383.
(52) Warren, B. E. X-Ray diffraction in random layer lattices. *Phys. Rev.* **1941**, *59*, 693–698.
(53) Drits, V. A.; Lanson, B.; Gaillot, A.-C. Birnessite polytype systematics and identification by powder X-ray diffraction. *Am. Mineral.* **2007**, *92*, 771–788.
(54) Grangeon, S.; Lanson, B.; Miyata, N.; Tani, Y.; Manceau, A. Structure of nanocrystalline phyllomanganates produced by freshwater fungi. *Am. Mineral.* **2010**, *95*, 1608–1616.
(55) Shannon, R. D. Revised effective ionic radii and systematic studies of interatomie distances in halides and chaleogenides. *Acta Crystallogr., Sect. A: Cryst. Phys., Diffr., Theor. Gen. Crystallogr.* **1976**, *32*, 751–767.
(56) Sposito, G. Cation exchange in soils: an historical and theoretical perspective. *ASA Spec. Publ.* **1981**, *40*, 13–30.
(57) Poinssot, C.; Baeyens, B.; Bradbury, M. H. Experimental and modelling studies of caesium sorption on illite. *Geochimica et Cosmochimica Acta* **1999**, *63*, 3217–3227.
(58) Tournassat, C.; Gailhanou, H.; Crouzet, C.; Braibant, G.; Gautier, A.; Gaucher, E. C. Cation exchange selectivity coefficient values on smectite and mixed-layer illite/smectite minerals. *Soil Science Society of America Journal* **2009**, *73*, 928–942.
(59) Staunton, S.; Roubaud, M. Adsorption of 137Cs on montmorillonite and illite: effect of charge compensating cation, ionic strength, concentration of Cs, K and fulvic acid. *Clays and Clay Minerals* **1997**, *45*, 251–260.
(60) Tremosa, J.; Arcos, D.; Matray, J.-M.; Bensenouci, F.; Gaucher, E. C.; Tournassat, C.; Hadi, J. Geochemical characterization and modelling of the Toarcian/Domerian porewater at the Tournemire underground research laboratory. *Applied Geochemistry* **2012**, *27*, 1417–1431.
(61) Steefel, C. I.; Carroll, S.; Zhao, P.; Roberts, S. Cesium migration in Hanford sediment: a multisite cation exchange model based on laboratory transport experiments. *Journal of Contaminant Hydrology* **2003**, *67*, 219–246.
(62) Miyata, S. Anion-exchange properties of Hydrotalcite-like compounds. *Clays Clay Miner.* **1983**, *31*, 305–311.
(63) Tournassat, C.; Bourg, I. C.; Steefel, C. I.; Bergaya, F. Chapter 1 - Surface properties of clay minerals; In *Natural and engineered clay barriers*; Tournassat, C.; Steefel, C. I.; Bourg, I. C.; Bergaya, F., Eds.; Developments in Clay Science; Elsevier, 2015; Vol. 6, pp. 5–31.
(64) Alidokht, L.; Oustan, S.; Khataee, A.; Neyshabouri, M. R.; Reyhanitabar, A. Enhanced removal of chromate by graphene-based sulfate and chloride green rust nanocomposites. *J. Taiwan Inst. Chem. Eng.* **2016**, *68*, 266–274.
(65) Christiansen, B. C.; Geckeis, H.; Marquardt, C. M.; Bauer, A.; Römer, J.; Wiss, T.; Schild, D.; Stipp, S. L. S. Neptunyl (NpO_2^+) interaction with green rust, GRNa,SO4. *Geochim. Cosmochim. Acta* **2011**, *75*, 1216–1226.
(66) Mitsunobu, S.; Takahashi, Y.; Sakai, Y.; Inumaru, K. Interaction of Synthetic Sulfate Green Rust with Antimony(V). *Environ. Sci. Technol.* **2009**, *43*, 318–323.
(67) Ona-Nguema, G.; Morin, G.; Wang, Y.; Menguy, N.; Juillot, F.; Olivi, L.; Aquilanti, G.; Abdelmoula, M.; Ruby, C.; Bargar, J. R.; Guyot, F.; Calas, G.; Brown, G. E. Arsenite sequestration at the surface of nano-$Fe(OH)_2$, ferrous-carbonate hydroxide, and green-rust after bioreduction of arsenic-sorbed lepidocrocite by Shewanella putrefaciens. *Geochim. Cosmochim. Acta* **2009**, *73*, 1359–1381.

(68) Randall, S. R.; Sherman, D. M.; Ragnarsdottir, K. V. Sorption of As(V) on green rust ($Fe_4(II)Fe_2(III)(OH)_{12}SO_4$ - $3H_2O$) and lepidocrocite (γ-FeOOH): Surface complexes from EXAFS spectroscopy. *Geochim. Cosmochim. Acta* **2001**, *65*, 1015–1023.
(69) Wang, Y.; Morin, G.; Ona-Nguema, G.; Juillot, F.; Guyot, F.; Calas, G.; Brown, G. E. J. Evidence for different surface speciation of arsenite and arsenate on green rust: An EXAFS and XANES study. *Environ. Sci. Technol.* **2010**, *44*, 109–115.
(70) Hansen, H. C. B.; Guldberg, S.; Erbs, M.; Bender Koch, C. Kinetics of nitrate reduction by green rusts—effects of interlayer anion and Fe(II):Fe(III) ratio. *Appl. Clay Sci.* **2001**, *18*, 81–91.
(71) Forano, C.; Costantino, U.; Prévot, V.; Gueho, C. T. Chapter 14.1 - Layered Double Hydroxides (LDH); In *Handbook of Clay Science*; Bergaya, F.; Lagaly, G., Eds.; Developments in Clay Science; Elsevier, 2013; Vol. 5, pp. 745–782.